

Model Predictive Direct Power Control for Grid-Connected Neutral-Point-Clamped Converters

James Scoltock, *Member, IEEE* Tobias Geyer, *Senior Member, IEEE*, and
Udaya K. Madawala, *Senior Member, IEEE*

Abstract—This paper presents a model predictive direct power control (MPDPC) scheme for high-power grid-connected neutral-point-clamped converters. The controller regulates the instantaneous real and reactive power, as well as the neutral-point potential of the converter, within a set of symmetrical bounds, whilst at the same time minimising the switching frequency of the converter. The proposed approach is distinct from previous predictive power control strategies in that a long prediction horizon is used, allowing lower device switching frequencies to be achieved. A detailed model of the system is provided and the control algorithm is discussed. Simulation results validate the applicability of the controller to a 3 kV, 6.72 MVA system. Experimental results, which are presented for a 240 V, 1.68 kVA prototype, show good agreement with those obtained in simulation and further validate the concept.

Index Terms—Direct power control, model predictive control, neutral-point-clamped converter

I. INTRODUCTION

OVER the last decade, the use of Model Predictive Control (MPC) [1] in power electronics applications has grown substantially, providing a viable alternative to the established control paradigms [2] - [6]. In particular, the Finite Control Set-MPC (FCS-MPC) approach has become very well-known [4] - [8]. FCS-MPC eschews a Pulse-Width Modulation (PWM) stage, and instead approaches the control task as an on-line optimisation problem. At each time-step, the switching state that is predicted to minimise a given cost function is applied to the converter. The FCS-MPC cost function usually incorporates a linear or quadratic penalty on output error [9], and may include additional terms penalising, for instance, device switching frequency [10].

Several FCS-MPC-based strategies have been proposed for grid-connected converters, with a number of these directly regulating the real and reactive power delivered to (or drawn from) the grid, e.g. [11] - [14]. Slightly different approaches are presented in [15] - [17]. Such approaches can be regarded as extensions of the Direct Power Control (DPC) concept [18], with the look-up operation replaced by an on-line optimisation algorithm. The first such approach was presented for the

control of a two-level active-front end in [11], and further developed in [12]. In [13], a strategy which is based on duty cycle control is presented. In [14], a strategy which is designed for a Medium-Voltage (MV) four-level diode-clamped converter is proposed. In addition to grid-connected converters, FCS-MPC strategies have also been developed for stand-alone applications [19] and machine drives [20].

An alternative MPC-based approach has emerged in parallel with FCS-MPC. Model Predictive Direct Torque Control (MPDTC), presented in [21] - [24], was developed specifically for the control of induction machine drives. By regulating the electromagnetic torque and stator flux magnitude within a given set of bounds, and by utilising the concept of trajectory extension, MPDTC is able to achieve prediction horizons of up to 100 time-steps [25]. This allows MPDTC to achieve very low device switching frequencies, making it very well-suited to MV applications, where reducing the switching frequency is an important objective. A natural extension of MPDTC is Model Predictive Direct Current Control (MPDCC), where the stator currents are directly regulated [26]. A recent review of direct MPC strategies with long prediction horizons is presented in [2].

This paper presents Model Predictive Direct Power Control (MPDPC), a new approach to the control of grid-connected converters, which regulates the instantaneous real and reactive power delivered to the grid within a set of symmetrical bounds, whilst minimising the device switching frequency of the converter. The use of a multi-step prediction horizon distinguishes MPDPC from the FCS-MPC-based strategies presented in [11] - [14]. The key benefit of MPDPC is the ability to achieve average device switching frequencies of well under 500 Hz whilst remaining within the acceptable limits of grid current harmonic distortion. Although some FCS-MPC-based controllers have also been shown to reduce the device switching frequency for MV grid-connected applications, e.g. [14], these approaches may still result in average device switching frequencies in excess of 500 Hz.

Simulation results, which are provided for a 3 kV, 6.72 MVA case study, verify the applicability of MPDPC to a high-power grid-connected Neutral-Point-Clamped (NPC) converter. By investigating the tuning of the controller, we demonstrate the conditions that yield the best level of performance for MPDPC. Subsequently, it is shown that at the chosen operating point the proposed MPDPC strategy is capable of offering lower device switching frequencies than FCS-MPC-based power control, with a reduction of up to 36% exhibited at the chosen steady-state operating point. A simplified implementation strategy is proposed, and experimental results are presented for a 240 V,

Manuscript submitted July 1, 2014; revised October 22, 2014; accepted for publication January 27, 2015.

Copyright ©2015 IEEE. Personal use of this material is permitted. However, permission to use this material for any other purposes must be obtained from the IEEE by sending a request to pubs-permissions@ieee.org.

J. Scoltock is with the School of Electrical and Electronic Engineering, The University of Manchester, M13 9PL Manchester, United Kingdom (email: james.scoltock@manchester.ac.uk)

T. Geyer is with ABB Corporate Research, 5405 Baden-Dättwil, Switzerland (email: t.geyer@ieee.org).

U.K. Madawala is with the Department of Electrical and Computer Engineering, The University of Auckland, 1010 Auckland, New Zealand (email: u.madawala@auckland.ac.nz).

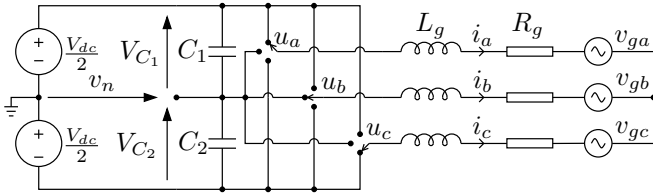


Fig. 1: Representation of a three-phase neutral-point-clamped converter connected to the grid.

1.68 kVA prototype. The per-unit (p.u.) values from the MV case-study are preserved, enabling direct comparison between simulation and experimental results. The experimental results exhibit excellent agreement with equivalent simulation results, providing support for the practical feasibility of MPDPC. Although the MPDPC concept was initially proposed in [27], issues relating to controller tuning, implementation strategies, and experimental evaluation have not yet been addressed. These are significant practical concerns, and as such this paper makes an important contribution by addressing these issues.

II. SETUP AND CONTINUOUS-TIME MODELLING

A representation of the system under consideration, which consists of a three-phase NPC converter connected to the grid via an L -filter, is shown in Fig. 1. The converter switching state is denoted $u_{abc} = [u_a \ u_b \ u_c]^T \in \{-1, 0, 1\}^3$, the three-phase grid current vector $i_{abc} = [i_a \ i_b \ i_c]^T$, and the three-phase grid voltage vector $v_{g,abc} = [v_{ga} \ v_{gb} \ v_{gc}]^T$. All modelling assumes that the direction of power flow is from converter to grid. The total DC-link voltage is given by the sum of the voltages across the upper and lower capacitors, i.e. $V_{dc} = V_{C_1} + V_{C_2}$. The neutral-point potential, v_n , is defined relative to the mid-point of the DC-link, and is given by $v_n = (V_{C_2} - V_{C_1})/2$, which under balanced conditions, when $V_{C_1} = V_{C_2}$, is zero. The dynamics of v_n can be described according to

$$\frac{dv_n}{dt} = \frac{1}{2C_{dc}} |u_{abc}|^T i_{abc} \quad (1)$$

where $C_1, C_2 = C_{dc}$ and $|u_{abc}| = [|u_a| \ |u_b| \ |u_c|]^T$. For a three-wire system, such that $i_a + i_b + i_c \triangleq 0$, v_n is only affected when one or two of the switching states are equal to zero.

Variables $\xi_{abc} = [\xi_a \ \xi_b \ \xi_c]^T$ in the three-phase abc reference frame are transformed to $\xi = [\xi_\alpha \ \xi_\beta]^T$ in the orthogonal $\alpha\beta$ reference frame through $\xi = \frac{2}{3}P\xi_{abc}$, where P is the transformation matrix

$$P = \begin{bmatrix} 1 & -\frac{1}{2} & -\frac{1}{2} \\ 0 & \frac{\sqrt{3}}{2} & -\frac{\sqrt{3}}{2} \end{bmatrix}. \quad (2)$$

Conversely, ξ can be transformed to ξ_{abc} via $\xi_{abc} = P^T\xi$.

Having modelled the internal dynamics of the converter and related the abc and $\alpha\beta$ reference frames, the converter switching state, u_{abc} , can be related to the $\alpha\beta$ -frame voltage at the terminals of the converter, $v = [v_\alpha \ v_\beta]^T$. As a first step, u_{abc} can be converted to a corresponding abc -frame output voltage vector, $v_{abc} = [v_a \ v_b \ v_c]^T$, via

$$v_m = \begin{cases} \frac{u_m V_{dc}}{2} & \text{if } u_m \in \{-1, 1\} \\ v_n & \text{if } u_m = 0 \end{cases}, \quad m \in \{a, b, c\}. \quad (3)$$

where v_a, v_b and v_c are defined relative to the mid-point of the DC-link. Subsequently, v_{abc} can be converted to v through $v = \frac{2}{3}Pv_{abc}$. For the sake of brevity, a function mapping u_{abc} to v will be denoted $v = f_v(u_{abc}, V_{dc}, v_n)$. Next, the continuous-time dynamics of the grid currents and grid voltages can be expressed as

$$\frac{dx}{dt} = Ax + Bv = Ax + Bf_v(u_{abc}, V_{dc}, v_n) \quad (4)$$

where the vector x is composed of the $\alpha\beta$ -frame grid current and voltage vectors, $i = [i_\alpha \ i_\beta]^T$ and $v_g = [v_{g\alpha} \ v_{g\beta}]^T$, such that

$$x = [i^T \ v_g^T]^T = [i_\alpha \ i_\beta \ v_{g\alpha} \ v_{g\beta}]^T \quad (5)$$

and where the matrices A and B are given by

$$A = - \begin{bmatrix} \frac{R_g}{L_g} & 0 & \frac{1}{L_g} & 0 \\ 0 & \frac{R_g}{L_g} & 0 & \frac{1}{L_g} \\ 0 & 0 & 0 & \omega \\ 0 & 0 & -\omega & 0 \end{bmatrix}, \quad B = \begin{bmatrix} \frac{1}{L_g} & 0 \\ 0 & \frac{1}{L_g} \\ 0 & 0 \\ 0 & 0 \end{bmatrix} \quad (6)$$

where L_g is the filter inductance, R_g the filter resistance, and $\omega = 2\pi f$, where f is the frequency of the grid. It should be noted that the state equation assumes the grid voltages to be balanced. Although not considered in this paper, the state-matrix A could be modified to also apply under unbalanced grid conditions, i.e. in the presence of grid faults. Several works have already proposed controllers which deal with this issue, refer to e.g. [28] for an overview. The instantaneous real and reactive power which are delivered to the grid, p and q , can be defined in terms of the $\alpha\beta$ -frame grid currents and voltages via [29]

$$p = \frac{3}{2}(i_\alpha v_{g\alpha} + i_\beta v_{g\beta}), \quad q = \frac{3}{2}(i_\alpha v_{g\beta} - i_\beta v_{g\alpha}). \quad (7)$$

III. MODEL PREDICTIVE DIRECT POWER CONTROL

A. Setup

The MPDPC setup is shown in Fig. 2. At each time-step k , the upper and lower DC-link capacitor voltages and the abc -phase grid currents and grid voltages are measured. The upper and lower capacitor voltages, collectively denoted $V_{C_{1,2}}(k)$, are used to determine $V_{dc}(k)$ and $v_n(k)$ via the simple expressions from the previous section. Similarly, the measured grid currents and grid voltages are converted from the abc -frame to the $\alpha\beta$ -frame to yield the vectors $i(k)$ and $v_g(k)$, respectively. These measured values are provided to the controller, along with the reference $p q^*(k) = [p^*(k) \ q^*(k)]^T$, with the controller determining the optimal input, $u(k)$, to apply to the converter. In the system under consideration, switching transitions between the upper and lower rails are prohibited and are not considered by the controller. Such restrictions are mandatory in industrial NPC converters in order to avoid shoot-through, see e.g. [23].

B. Internal Control Model

An internal control model which describes the dynamics of the system is a necessary component for MPC-based controllers [1]. For MPDPC, a discrete-time state-space model is used, with $t = kT_s$, where $t \in \mathbb{R}$ denotes (continuous)

time, $k \in \mathbb{N}_0$ denotes the current time-step, and T_s denotes the sampling interval. The input vector, $u(k)$, is defined as the three-phase switching state of the converter, i.e.

$$u(k) = u_{abc}(k) = [u_a(k) \ u_b(k) \ u_c(k)]^T. \quad (8)$$

Due to the differing nature of the dynamics of the neutral-point potential and the grid currents and voltages (see (1) and (4)), it is convenient to utilise two (coupled) discrete-time models. The first, which describes the non-linear discrete-time dynamics of the neutral-point potential, is based on forward-Euler discretisation. By recalling (1), (2) and (5) and noting that

$$\frac{dv_n}{dt} \approx \frac{1}{T_s} (v_n(k+1) - v_n(k)) \quad (9)$$

it is possible to state that

$$v_n(k+1) = \frac{T_s}{2C_{dc}} |u(k)|^T [P^T \ 0_{3 \times 2}] x(k) + v_n(k) \quad (10)$$

with $x(k)$ defined in the same manner as (5) and where $0_{3 \times 2}$ denotes the 3×2 zero matrix. The linear dynamics described by (4) can be discretised by applying a zero-order hold to the neutral-point potential over the sampling interval T_s , through which the discrete-time dynamics of the state vector are given by

$$x(k+1) = Fx(k) + Gf_v(u(k), V_{dc}(k), v_n(k)) \quad (11)$$

with F and G given by

$$F = e^{AT_s}, \quad G = A^{-1}(F - I_{4 \times 4})B \quad (12)$$

and where $I_{4 \times 4}$ denotes the 4×4 identity matrix. Because the sampling frequency $1/T_s$ (in the range of 10 - 40 kHz) is significantly higher than the switching frequency (in the range of 200 - 500 Hz), the dynamics of the neutral-point potential are relatively slow, and the switching state is always held constant between sampling instants, (11) can be regarded as constituting a near-exact discrete-time model for the purposes of MPDPC. Finally, the discrete-time output vector, which contains the variables that the controller seeks to directly regulate, is given by

$$y(k) = [p(k) \ q(k) \ v_n(k)]^T \quad (13)$$

which, by recalling (7), is easily defined as

$$y(k) = \begin{bmatrix} \frac{3}{2}(x_1(k)x_3(k) + x_2(k)x_4(k)) \\ \frac{3}{2}(x_1(k)x_4(k) - x_2(k)x_3(k)) \\ v_n(k) \end{bmatrix} \quad (14)$$

where $x_n(k)$ denotes the n -th element of the vector $x(k)$. The above model can be applied at any time-step within a prediction, such that k can be substituted with $k + \ell$. Note that the model assumes that the DC-link voltage remains constant for the duration of each prediction, i.e. $V_{dc}(k + \ell) = V_{dc}(k)$, $\forall \ell \in \{0, 1, \dots, N_p - 1\}$.

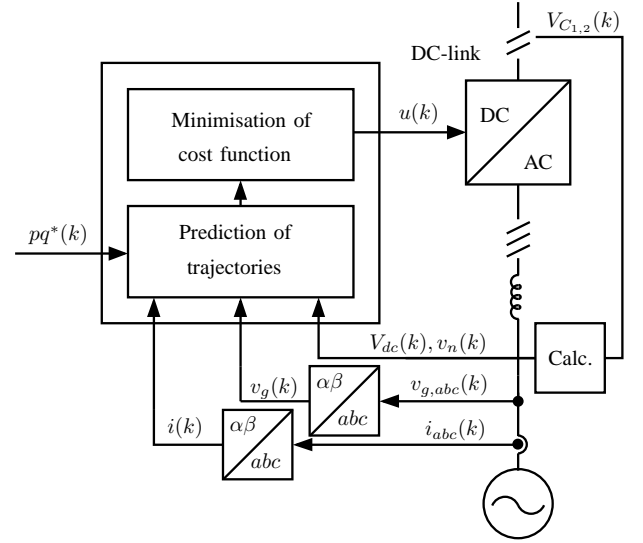


Fig. 2: Basic setup for model predictive direct power control for a three-phase neutral-point-clamped converter connected to the grid.

C. Control Objectives and Procedure

The primary objective of MPDPC is directly inherited from conventional DPC; namely, to regulate the real and reactive power within a set of symmetrical bounds defined about the respective references, p^* and q^* . For the NPC converter, the controller is also required to regulate the neutral-point potential. This is achieved in the same manner as MPDTC [22], with a set of symmetrical bounds defined about the neutral-point potential reference, $v_n^* \triangleq 0$. Thus, the controller aims to ensure that the following constraints are satisfied

$$|m^*(k) - m(k)| \leq \delta_m, \quad m \in \{p, q, v_n\}. \quad (15)$$

The secondary objective is to minimise the switching frequency of the converter, which is achieved by minimising the switching commutations over time. Unlike most formulations of predictive power control, which utilise a fixed prediction horizon of one time-step, i.e. $N_p \triangleq 1$, MPDPC instead utilises a switching horizon, N_s , of fixed length, giving rise to prediction horizons of varying length. The switching horizon contains an ordered sequence of events which take place within each prediction: switch, denoted by ‘S’, and extend, denoted by ‘E’. When an ‘S’ event occurs, the controller has the freedom to switch from the current input to a new input, advancing the prediction horizon by one time-step. When an ‘E’ event occurs, the input is held constant, with the state and output trajectories extended until violation of the output constraints is predicted to occur, advancing the prediction horizon by a variable number of time-steps. Note that a lower case ‘e’ event can be included at the beginning of the switching horizon; this represents an ‘optional’ extension step before the first ‘S’ event. One can thus consider the switching horizons $N_s = \text{‘SSE’}, \text{‘eSE’}, \text{‘eSESE’}, \text{‘eSESESE’}$ and so on. For each candidate input sequence $U^j(k) = [u^j(k) \dots u^j(k + N_p^j - 1)]$, $j \in \mathcal{J}_c$, where \mathcal{J}_c contains the indices of all candidate input sequences, the cost is given by the number of switching

transitions divided by the prediction horizon, i.e.

$$c^j = \sum_{\ell=0}^{N_p^j-1} \frac{\|w^j(k+\ell) - w^j(k+\ell-1)\|_1}{N_p^j}. \quad (16)$$

If there are no candidate input sequences, i.e. $\mathcal{J}_c = \emptyset$, the cost is determined through a modified approach. Each allowable input $u^j(k)$, $j \in \mathcal{J}_{dl}$, where \mathcal{J}_{dl} contains the indices of all allowable inputs at time-step k , is considered. With the error vector ϵ^j defined as the normalised deviation of the output vector from its reference, i.e.

$$\epsilon^j = \text{diag}(1/\delta_p, 1/\delta_q, 1/\delta_{v_n}) \times (|y^*(k+1) - y^j(k+1)|) \quad (17)$$

where $y^*(k+1) = [p^*(k+1) \ q^*(k+1) \ 0]^T$, the cost for each input is computed according to

$$c_{dl}^j = \|\epsilon^j\|_\infty. \quad (18)$$

Finally, the index of the optimal input sequence is found via

$$j = \arg \min_{j \in \mathcal{J}_c} c^j \quad \text{or} \quad j = \arg \min_{j \in \mathcal{J}_{dl}} c_{dl}^j. \quad (19)$$

with the first input of the sequence, $u(k) = u^j(k)$, applied to the converter. Further details are omitted due to space constraints; a more detailed explanation of the MPDPC algorithm can be found in [27], with the MPDTC algorithm, from which MPDPC is descended, discussed in detail in [21] - [24].

IV. SIMULATION RESULTS

In this section, simulation results are presented for a 3 kV, 6.72 MVA system, with additional ratings and parameters provided in Table I. The first purpose of the results is to examine the performance of the controller as the real and reactive power bounds, δ_p and δ_q , are varied. The second is to validate the steady-state performance of MPDPC by benchmarking it against different control strategies; namely Voltage-Oriented Control (VOC) with Space Vector Modulation (SVM), and FCS-MPC-based power control. The results in this section evaluate the controllers under ‘best-case’ conditions; the grid voltage is treated as being ideal and is free of harmonics and amplitude/frequency variation. Controller delay is treated as being negligible, and measurements are free of offset and noise. For MPDPC, the sampling interval is fixed at $T_s = 25 \mu\text{s}$; this is typically used when evaluating the performance of MPDxC in simulation, see e.g. [30], and it should be noted that for MPDPC, a relatively narrow sampling interval of 25

TABLE I: RATINGS AND PARAMETERS OF THE MEDIUM-VOLTAGE AND LOW-VOLTAGE SYSTEMS.

Ratings and Parameters			
Quantity	MV value	LV value	p.u. value
DC-link voltage, V_{dc}	5 kV	400 V	2.041
Grid line-to-line voltage, V_g	3 kV	240 V	1.225
Grid current, I_g	1.29 kA	4.04 A	0.707
Grid power, P_g	6.72 MVA	1.68 kVA	1.000
Grid frequency, f	50 Hz	50 Hz	1.000
DC-link capacitance, C_{dc}	10 mF	390 mF	4.200
Inductance, L_g	1.13 mH	29 mH	0.266
Resistance, R_g	20 m Ω	0.5 Ω	0.015

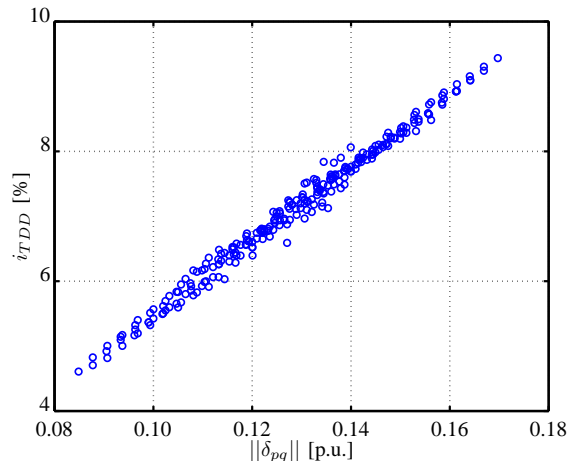


Fig. 3: Grid current distortion against $\|\delta_{pq}\|$ for $N_s = \text{‘eSE’}$.

- 50 μs is necessary in order for the benefit of medium-to-long switching horizons to be fully realised. Because the total DC-link voltage V_{dc} is treated as being constant, outer control loops are not used. For all results the real power reference is $p^* = 1$ p.u. whilst the reactive power reference is $q^* = 0$ p.u..

A. Tuning

Unlike FCS-MPC, where the issue of controller tuning primarily relates to the assignment of weighting terms within the cost function [9], the tuning of MPDPC is concerned with the assignment of appropriate values to the real and reactive power bounds, δ_p and δ_q . In general, wider bounds lead to higher values of grid current Total Demand Distortion (TDD) and lower switching frequencies, with the reverse being true for narrower bounds. Although the neutral-point potential is also regulated within a set of bounds, the bound width δ_{v_n} is usually fixed at around 0.03 p.u. and is not considered when tuning the controller. In this section, we define $\delta_{pq} = [\delta_p \ \delta_q]^T$.

Fig. 3 shows the grid current TDD, i_{TDD} , against the Euclidean-norm of the bounds, $\|\delta_{pq}\| = \sqrt{\delta_p^2 + \delta_q^2}$, when varying δ_p and δ_q between 0.06 and 0.12 p.u. with $N_s = \text{‘eSE’}$. It is clear that there is a linear relationship between $\|\delta_{pq}\|$ and the grid current TDD, with the value of $\|\delta_{pq}\|$ being the main parameter that is responsible for determining i_{TDD} . This is further illustrated in Table II, which shows the grid current TDD for $\|\delta_{pq}\| = 0.12$ p.u., with different combinations of δ_p and δ_q and with $N_s = \text{‘eSE’}$, ‘eSESE’ and ‘eSESESE’. The values of TDD that are summarised in Table II further support the assertion that the value of $\|\delta_{pq}\|$ is the main parameter that is responsible for controlling the value of i_{TDD} , with the

TABLE II: REAL AND REACTIVE POWER BOUNDS AND ASSOCIATED GRID CURRENT DISTORTION WITH DIFFERENT SWITCHING HORIZONS.

Bounds [p.u.]		i_{TDD} [%]		
δ_p	δ_q	eSE	eSESE	eSESESE
0.060	0.104	6.4	6.4	6.3
0.072	0.096	6.5	6.6	6.4
0.085	0.085	6.5	6.8	6.4
0.096	0.072	6.6	6.8	6.5
0.104	0.060	6.5	6.5	6.4

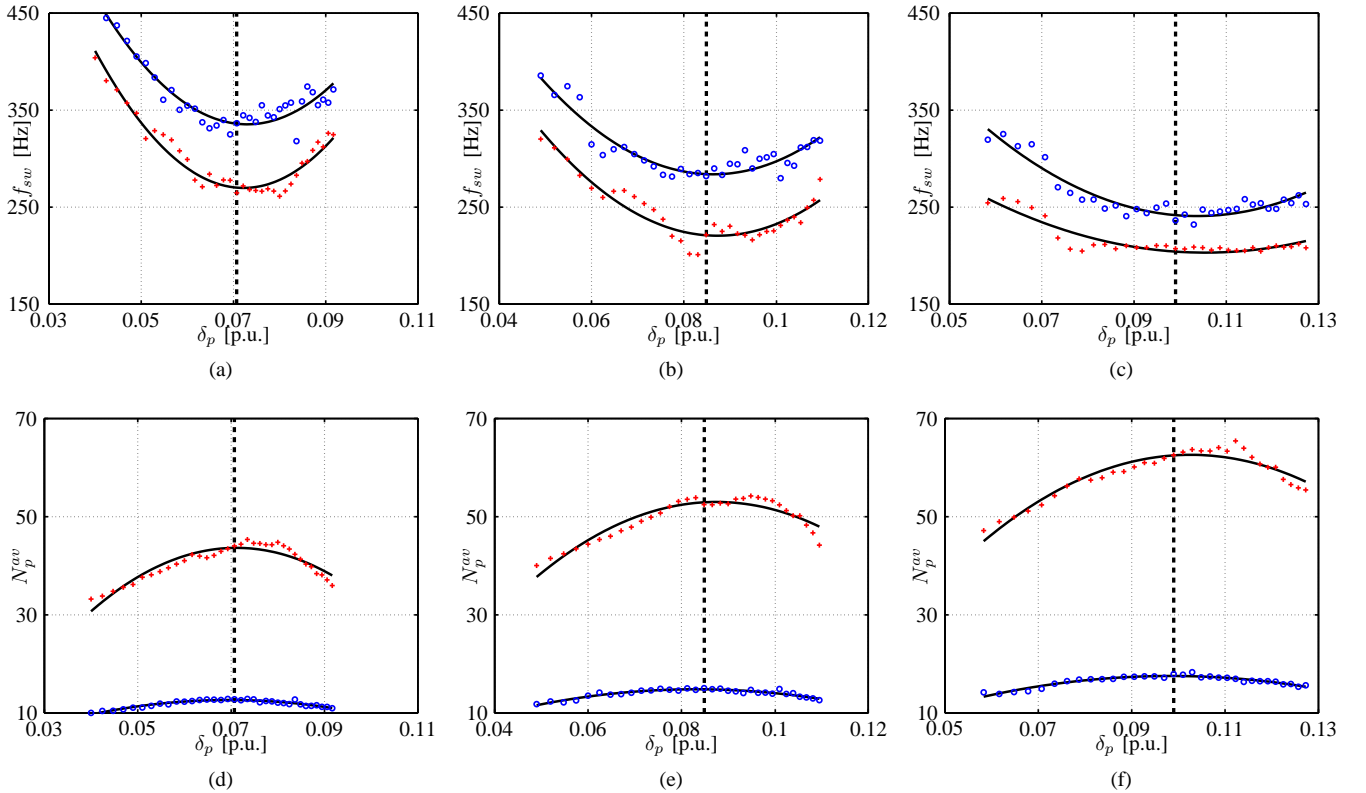


Fig. 4: Average device switching frequency (top row) and average prediction horizon (bottom row) against the width of the real power bound, δ_p , for different values of $\|\delta_{pq}\|$. Results for the switching horizons eSE (o) and eSESESE (+) are shown. $\|\delta_{pq}\| = 0.10$ p.u. (a) and (d), 0.12 p.u. (b) and (e), and 0.14 p.u. (c) and (f).

individual combination of δ_p and δ_q having little influence for a given value of $\|\delta_{pq}\|$.

Subsequently, we examine the relationship between the bounds and the average device switching frequency, f_{sw} . Fig. 4 shows how f_{sw} and the average prediction horizon (number of time-steps), N_p^{av} , change as δ_p is varied, for three different values of $\|\delta_{pq}\|$. The individual data points are shown along with second-order trend curves. For all values of $\|\delta_{pq}\|$, δ_p is gradually incremented with δ_q (not shown) correspondingly decremented. Fig. 4(a) shows the relationship between f_{sw} and δ_p with $\|\delta_{pq}\| = 0.1$ p.u. for both $N_s = \text{'eSE'}$ and 'eSESESE' . It is clear that as δ_p is initially incremented, f_{sw} decreases rapidly, before becoming much flatter as the values of δ_p and δ_q approach one another (the point at which $\delta_p = \delta_q$ is denoted by a thick dashed line). The trend curves for both switching horizons attain a minimum at approximately this point, before gradually increasing as δ_p is further increased. Fig. 4(d) shows how N_p^{av} changes for the same values of δ_p . For both switching horizons, N_p^{av} reaches a peak at approximately the same point as f_{sw} attains a minimum.

Figs. 4(b) and 4(e) show the same relationships with $\|\delta_{pq}\| = 0.12$ p.u.. For both switching horizons, the same trends are apparent, with f_{sw} reaching a minimum, and N_p^{av} a maximum, around the point where $\delta_p = \delta_q$. The same trends are also visible in Figs. 4(c) and 4(f) with $\|\delta_{pq}\| = 0.14$ p.u.. Note also that as $\|\delta_{pq}\|$ is increased, the average device switching frequencies decrease, whilst the average prediction horizons increase. Fig. 4 also highlights the improvement in

performance that is exhibited when the switching horizon is extended from 'eSE' to 'eSESESE', with the resulting increase in prediction horizon giving rise to lower switching frequencies.

The trends in Fig. 4 indicate that for a given value of $\|\delta_{pq}\|$, the best performance is approximately obtained when $\delta_p = \delta_q$. This is explained by the fact that 'square' bounds on the real and reactive power result in the same bounds being (implicitly) imposed on the dq -frame currents. For MPDPC, this provides the best approximation to (rotating) hexagonal bounds on the dq -frame grid currents, which as shown in [26] are optimal with respect to current distortion. Consequently, by imposing the constraint that $\delta_p \triangleq \delta_q$, the tuning process for MPDPC becomes relatively straightforward. Referring to the linear trend exhibited in Fig. 3 and with Δ denoting a change in a variable, it becomes possible to say that $\Delta i_{TDD} \approx \sqrt{2}K\Delta\delta_p, \sqrt{2}K\Delta\delta_q$, where $\|\delta_{pq}\| \triangleq \sqrt{2}\delta_p, \sqrt{2}\delta_q$, and where K is a constant of proportionality. For the system under consideration, it can be deduced from Fig. 3 that $K \approx 57$ for the range of $\|\delta_{pq}\|$ that is shown.

It should be noted that the linear relationship breaks down for very low or high values of $\|\delta_{pq}\|$. If $\|\delta_{pq}\|$ was reduced below a certain level, then the controller would reach a lower TDD limit, with a corresponding upper f_{sw} limit. Conversely, if $\|\delta_{pq}\|$ was raised to a certain point, it would enter six-step operation. The value of $\|\delta_{pq}\|$ that corresponds to the upper f_{sw} limit is determined by the sampling interval, T_s , the voltage margin between the DC-link voltage and the

TABLE III: SIMULATED STEADY-STATE PERFORMANCE COMPARISON OF VOC WITH SVM, FCS-MPC AND MPDPC. THE SECOND SECTION SHOWS ABSOLUTE VALUES, AND THE THIRD SECTION SHOWS PERCENTAGE VALUES RELATIVE TO VOC WITH SVM.

Control scheme	Control setting	Switching horizon, N_s	Average prediction horizon, N_p^{av}	i_{TDD} [%]	f_{sw} [Hz]	i_{TDD} [%]	f_{sw} [%]
VOC with SVM	$f_c = 750$ Hz	-	-	4.4	400	100	100
FCS-MPC	$\lambda_n = 3.8, \lambda_{f_{sw}} = 0.034$	-	$N_p \triangleq 1$	4.6	526	105	132
MPDPC	$\delta_p = \delta_q = 0.06$ p.u.	eSE	11	4.6	394	105	98.5
MPDPC	$\delta_p = \delta_q = 0.06$ p.u.	eSESE	24	4.5	356	102	89.0
MPDPC	$\delta_p = \delta_q = 0.06$ p.u.	eSESESE	37	4.6	335	105	83.8

magnitude of the grid voltage, and the values of L_g and R_g . If we treat the highest allowable average device switching frequency of an MV converter as being around 500 Hz, then for the system under consideration, the minimum acceptable value of $\|\delta_{pq}\|$ is around 0.05 p.u. for $N_s = \text{'eSE'}$. For $N_s = \text{'eSESE'}$ and $N_s = \text{'eSESESE'}$, the minimum acceptable value of $\|\delta_{pq}\|$ is slightly lower.

Under the assumption of unity power factor operation, the results relating to tuning can be regarded as general. This stems from the use of p.u. bounds, which are defined relative to the rated power, and the use of TDD, which expresses the harmonic components of the current as a percentage of the rated, rather than instantaneous, fundamental component [31]. As such, the trends shown in Figs. 3 and 4 would exhibit little variation with different values of p^* .

B. Steady-State Performance Evaluation

In order to evaluate the steady-state performance of the proposed MPDPC concept, it is compared against VOC with SVM and FCS-MPC-based power control. VOC is a well-known approach for the control of grid-connected converters, see e.g. [32], and the references therein, and thus constitutes an important benchmarking tool. The SVM modulation stage is implemented according to [33]. The FCS-MPC controller is implemented according to the method proposed in [12], [14], with the weighting terms in the cost function penalising the number of switching transitions, $\lambda_{f_{sw}}$, and the magnitude of the neutral-point potential, λ_n , as proposed for NPC converters in [10]. The sampling interval for FCS-MPC is $T_s = 100 \mu\text{s}$, which is used in [14]. The approach that is presented in [14] represents the current state-of-the-art for direct-MPC-based power control of MV grid-connected converters, and therefore forms another important benchmark when assessing the performance of MPDPC.

The strategies are compared in Table III. The carrier frequency, f_c , for SVM, the weighting terms for FCS-MPC, and the real and reactive power bounds for MPDPC are tuned such that the grid current TDD is fixed at approximately 4.5% for all strategies. The resulting average device switching frequency for VOC is 400 Hz. FCS-MPC results in an average device switching frequency of 526 Hz, significantly higher than that of VOC with SVM. With the switching horizon $N_s = \text{'eSE'}$, MPDPC is able to achieve approximately the same device switching frequency as VOC whilst offering a reduction in switching frequency of 25% compared to FCS-MPC. With the switching horizon extended to $N_s = \text{'eSESE'}$, MPDPC is able to offer a reduction in switching frequency of more than 10% compared to VOC and more than 32% compared to FCS-MPC, and with the switching horizon further extended to $N_s =$

'eSESESE' , MPDPC is able to offer a reduction in switching frequency of about 15% compared to VOC and 36% compared to FCS-MPC. Note that the average prediction horizon more than triples as the switching horizon is extended from 'eSE' to 'eSESESE' .

The reduction in steady-state switching frequency that is potentially afforded by MPDPC, relative to VOC and FCS-MPC, is an important advantage of the proposed strategy. This is because lower switching frequencies improve the efficiency of high-power converters, and may prevent the premature degradation or failure of devices such as the Integrated Gate-Commutated Thyristor (IGCT). As an alternative comparison, one could tune the controllers to achieve approximately the same switching frequency, under which circumstances MPDPC would offer a reduction in grid current TDD. This is shown for MPDCC in [26].

V. EXPERIMENTAL IMPLEMENTATION AND RESULTS

A. Setup

In this section, experimental results are provided in order to validate the practical applicability of the MPDPC concept. Results have been obtained using a down-scaled 240 V, 1.68 kVA system, with additional parameters provided in Table I. The Total Harmonic Distortion (THD) of the grid voltage, $v_{g,THD}$, was measured at approximately 1.5%, with the majority of the harmonic content concentrated at the 5th and 7th harmonics. Because the experimental prototype preserves the p.u. values from the MV setup, direct comparison with results obtained in simulation is possible. The DC-link is fed from a constant-voltage power supply. The upper and lower DC-link capacitor voltages and the abc -phase grid currents and grid voltages are directly sampled and fed to the controller. The control algorithm is implemented on the 150 MHz TMS320F28335 Digital Signal Processor (DSP). Gate signal and dead-time generation is handled by an Altera Cyclone II Field-Programmable Gate Array (FPGA). The DSP was programmed using C, and the FPGA was configured using VHDL. The same steady-state operating point that was used in simulation is retained, i.e. $p^* = 1$ p.u., $q^* = 0$ p.u..

B. Low-Complexity Algorithm

Because of the limited processing power of the available control platform, a modified approach is adopted. The switching horizon is limited to $N_s = \text{'eSE'}$ and the sampling interval is extended to $T_s = 100 \mu\text{s}$. Extension steps are carried out using Linear Extrapolation (LE), which was also used for MPDTC in [21] - [23]. Note that in order to compensate for the delay that is introduced by the controller, a delay compensation strategy is utilised [23], [34]. At time-step k , the optimal input

that was computed at the previous time-step is applied, with the measured states projected forward to $k+1$ and the optimal input to be applied at $k+1$ being determined. In this section $\xi(k+\ell|k)$ denotes a value at time-step $k+\ell$ which is calculated based on measurements obtained at time-step k . In order to further simplify the implementation, the control procedure is converted from a minimisation to a maximisation problem. This changes the cost function for a candidate input to

$$c^j = N_p^j \frac{1}{\Delta u^j} \quad (20)$$

with the optimal input index becoming

$$j = \arg \max_{j \in \mathcal{J}_c} c^j. \quad (21)$$

where $1/\Delta u^j$ denotes the inverse of the number of switching transitions between $u(k|k-1)$ and $u^j(k+1|k)$. The value of $1/\Delta u^j$ is retrieved from a look-up table. By adopting such an approach, the cost can be calculated without the use of division terms, which are expensive in the context of a DSP. The resulting algorithm is the following.

- 1) Sample the voltages of the DC-link and the *abc*-phase grid currents and grid voltages, and apply the previously calculated input, $u(k|k-1)$, to the converter.
- 2) Determine the neutral-point potential $v_n(k|k)$ and the state vector $x(k|k)$. Using the internal control model, calculate $x(k+1|k)$, $v_n(k+1|k)$ and $y(k+1|k)$ based on the input $u(k|k-1)$.
- 3) Using the internal control model, calculate $x(k+2|k)$, $v_n(k+2|k)$ and $y(k+2|k)$ with $u(k+1|k) = u(k|k-1)$. If each component of $y(k+2|k)$ is within its bound or moving closer to its reference, then set $u(k+1|k) = u(k|k-1)$ and proceed to Step 7. Else, proceed to Step 4.
- 4) Initiate the optimal costs as $c^{opt} = 0$ and $c_{dl}^{opt} = \infty$.
- 5) Determine the set of inputs $\mathcal{U}(k+1)$ that can be applied without violating the switching constraints of the converter (refer to Section III-A). Denote the set of allowable input indices as \mathcal{J} and initiate a working set $\mathcal{J}_w = \mathcal{J}$.
- 6a) Read out and remove the first index j from the working set \mathcal{J}_w . Using the internal control model, determine $x^j(k+2|k)$, $v_n^j(k+2|k)$ and $y^j(k+2|k)$ based on $u^j(k+1|k) \in \mathcal{U}(k+1)$.
- 6b) If the input is a candidate (refer to the definition provided in [27]), extrapolate each of the outputs to determine the prediction horizon N_p^j . Determine $1/\Delta u^j$ via the look-up table and compute the cost, c^j , according to (20). If $c^j > c^{opt}$, set $c^{opt} = c^j$ and $u(k+1|k) = u^j(k+1|k)$.
- 6c) If the input is not a candidate and $c^{opt} = 0$, calculate c_{dl}^j according to (18). If $c_{dl}^j < c_{dl}^{opt}$, set $c_{dl}^{opt} = c_{dl}^j$ and $u(k+1|k) = u^j(k+1|k)$.
- 6d) If $\mathcal{J}_w \neq \emptyset$, return to Step 6a. Else, proceed to Step 7.
- 7) Retain $u(k+1|k)$ for application at the next time-step, where $k \leftarrow k+1$.

Unlike the algorithm proposed for MPDTC in [23], the optimal cost and input is successively updated after the prediction

horizon is computed for each candidate input. Similarly, if an input is not a candidate, the optimal cost and input under deadlock is updated if no candidate inputs have yet been found, i.e. $c^{opt} = 0$. This avoids the need for costs and/or predicted outputs to be stored, making implementation more straightforward.

C. Performance Evaluation

Fig. 5 shows the experimental waveforms obtained with $\delta_p = \delta_q = 0.06$ p.u.. Figs. 5(a) and 5(b) show the real and reactive power, respectively, over one fundamental period. Note that due to the presence of measurement noise and sensor delay, the outputs sometimes move slightly outside their respective bounds. However, these deviations are quickly corrected and do not affect the mean values of the real and reactive power, both of which were found to be within 1% of their references. Fig. 5(c) shows the regulation of the neutral-point potential. Figs. 5(d) and 5(e) show the grid currents and grid current spectrum, respectively. The main peaks in the spectrum are the 5th, 7th, 11th, 13th and 23rd harmonics. Note also that a small 2nd harmonic component, as well as 3rd and 9th harmonic components, are also visible. In PWM-based three-phase setups, the latter are not usually seen, however for MPDPC, where the switching pattern differs between the three phases, as shown in Fig. 5(f), it is possible for triplen harmonics to emerge. Note however that all of the harmonics that are present are within the limits recommended by IEEE Standard 519 [31]. When averaged over 0.2 s, the average device switching frequency is 428 Hz, whilst the grid current TDD is 4.9%, which is also within the limit of 5% that IEEE Standard 519 sets for overall grid current TDD.

Table IV compares the experimental performance of MPDPC against the performance obtained in simulation with $N_s = \text{'eSE'}$. The simulation results differ slightly from those presented in Section IV, as the sampling interval is extended to 100 μs , and 5th and 7th harmonics are added to the grid voltage to give the same value of $v_{g,THD}$ that is present experimentally. It can be seen that by tuning the bounds appropriately, the performance at each point under consideration is very similar under both experimental and simulated conditions. Because of the bound violation that sometimes occurs experimentally due to noise and delay, the bounds need to be slightly wider in simulation in order to achieve the equivalent performance. Nonetheless, the results match very well and validate the practical validity of MPDPC. Note also that the rate at which i_{TDD} increases with δ_p and δ_q closely matches that which is predicted from Fig. 3 for both the experimental and simulated results. This indicates that the tuning results from Section IV are valid in a practical setting.

Fig. 6 shows the response of MPDPC in the presence of reference steps. The bounds that were used in Fig. 5 are retained. At $t = 10$ ms, the real power reference drops from 1 to 0 p.u.. The controller responds well, with the real power reaching the desired level in about 1.5 ms. At $t = 30$ ms, the reference changes back to 1 p.u., with the real power reaching the desired level within about 3.5 ms. Observe that the reactive power remains well-regulated during the transients, and the real power and current trajectories are free of overshoot and

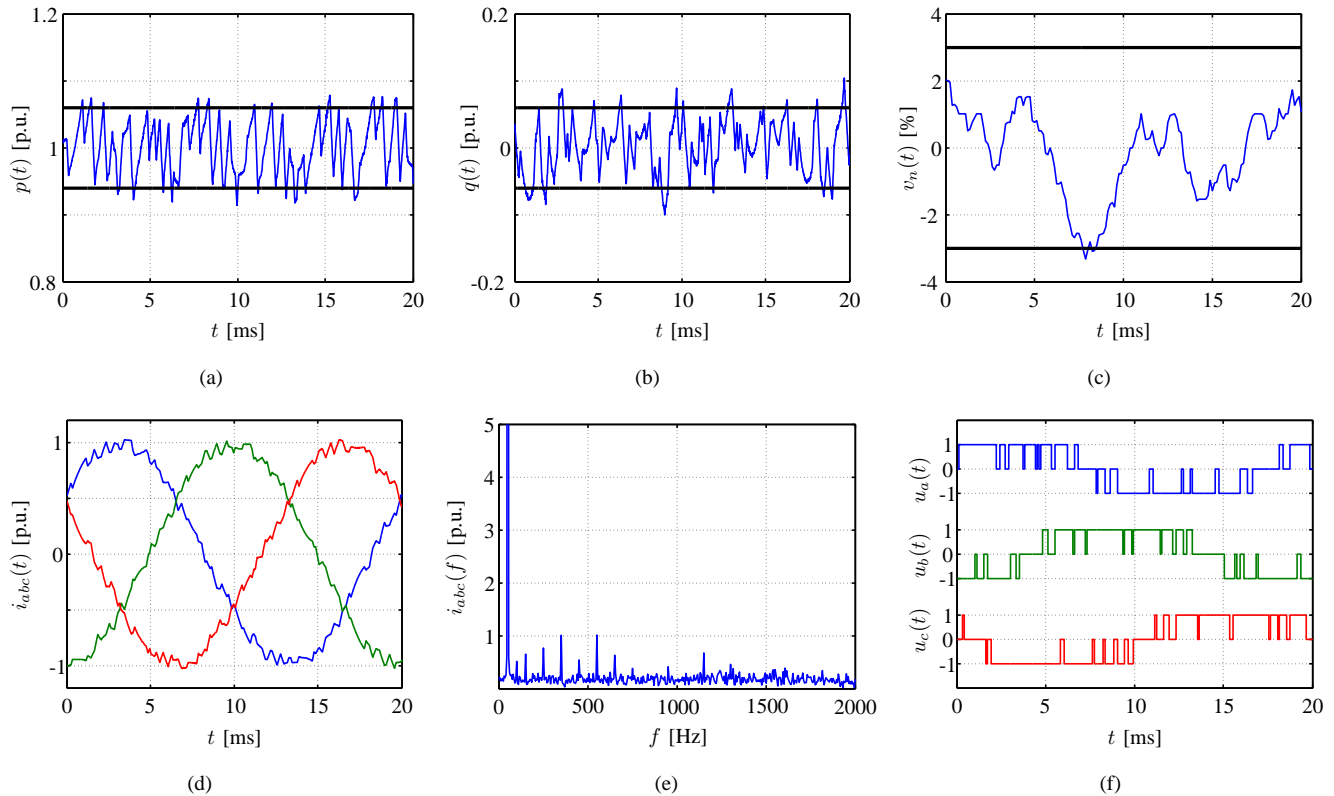


Fig. 5: Experimental performance of MPDPC with the switching horizon $N_s = \text{'eSE'}$ and bounds of $\delta_p = \delta_q = 0.06$ p.u.. Real power (a), reactive power (b), neutral-point potential (c), grid currents (d), grid currents spectrum (e), and inputs (f)

TABLE IV: COMPARISON OF EXPERIMENTAL AND SIMULATED PERFORMANCE OF MPDPC WITH $N_s = \text{'ESE'}$, $T_s = 100 \mu\text{s}$, AND $v_{g,THD} = 1.5\%$.

Experimental			Simulation		
Bounds [p.u.]	f_{sw} [Hz]	i_{TDD} [%]	Bounds [p.u.]	f_{sw} [Hz]	i_{TDD} [%]
$\delta_p = \delta_q = 0.060$	428	4.9	$\delta_p = \delta_q = 0.066$	424	4.8
$\delta_p = \delta_q = 0.080$	285	6.6	$\delta_p = \delta_q = 0.086$	290	6.3
$\delta_p = \delta_q = 0.100$	228	8.0	$\delta_p = \delta_q = 0.106$	230	8.2
$\delta_p = \delta_q = 0.120$	196	9.7	$\delta_p = \delta_q = 0.126$	200	9.5

ringing. It should be noted that the response when moving from 0 to 1 p.u. is somewhat slower due to the fact that the available voltage margin is very narrow; this is also observed in a recent work for a MV machine drive with a similar p.u. stator inductance and voltages [35]. The experimental response times are consistent with those that have been observed in simulation for a similarly-rated system [27], validating the transient performance of MPDPC.

D. Discussion

Although the experimental validation of MPDPC has been limited to the switching horizon $N_s = \text{'eSE'}$, the results nonetheless indicate that MPDPC is a viable concept. With $\delta_p = \delta_q = 0.06$ p.u., both the average device switching frequency and grid current TDD of MPDPC are well-within practical limits. Although the experimental switching frequency achieved by MPDPC is slightly higher than the simulated switching frequency of SVM from Table III, it should be observed that the switching frequency is almost 20% lower than the simulated switching frequency of 526 Hz achieved by FCS-MPC-based power control, with the grid current TDD being

only marginally higher.

Recently, it has been shown that with a more powerful control platform and by adopting parallel computing techniques, it is possible for the MPDPC algorithm to be executed in real-time with lengthened switching horizons and a sampling interval of $T_s = 25 \mu\text{s}$ [36]. Such an approach could also be adopted for MPDPC, and based on the experimental results that have been presented in this section for $N_s = \text{'eSE'}$, which show a very good level of agreement with the equivalent simulation results, it is reasonable to expect the experimental performance with longer switching horizons, and a narrower sampling interval, to closely match that obtained in simulation. This would enable very significant practical improvements over VOC with SVM to be achieved.

This work has focused on the application of MPDPC to a balanced three-phase grid. As mentioned in Section II, the discrete-time model could be modified to describe the dynamics in the case of an unbalanced grid voltage. The output equation is valid under unbalanced conditions, and as such the outputs could be regulated as desired. Although model mismatch, e.g. grid inductance variation, has not been considered,

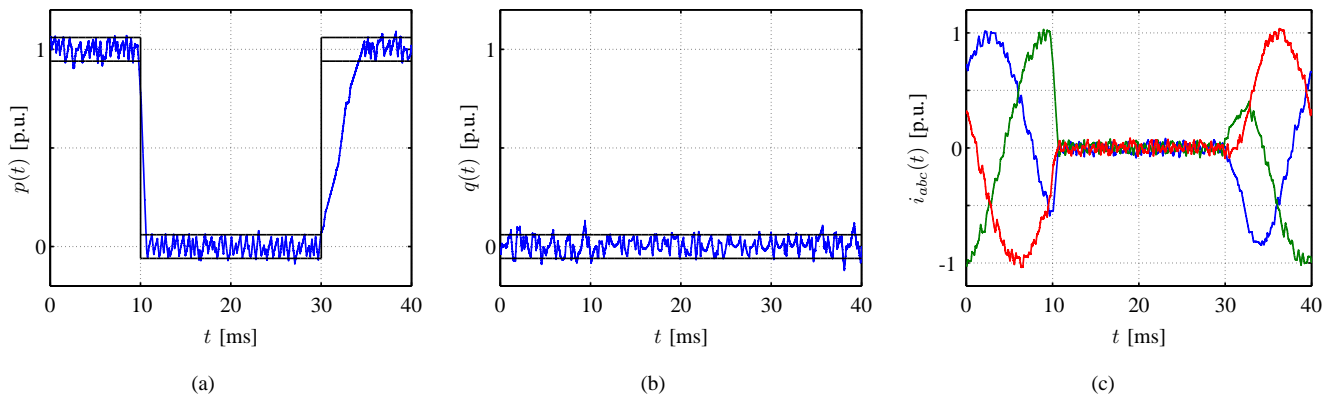


Fig. 6: Experimental performance of MPDPC under transient conditions with the switching horizon $N_s = \text{'eSE'}$ and bounds of $\delta_p = \delta_q = 0.06$ p.u.. Real power (a), reactive power (b), and grid currents (c).

it is well-established that MPC is robust to parameter variation. The robust stability of MPDCC is demonstrated in [37], and similar reasoning could be applied to validate the robustness of MPDPC in the presence of model mismatch.

VI. CONCLUSIONS

This paper has presented a Model Predictive Direct Power Control (MPDPC) scheme for high-power grid-connected NPC converters. Simulation results were presented in order to validate the applicability of MPDPC to a 3 kV, 6.72 MVA system. Trade-off curves demonstrated the performance characteristics of MPDPC as the real and reactive power bounds are varied, and it was shown that the steady-state performance of MPDPC is capable of significantly improving upon that of VOC with SVM and FCS-MPC-based power control. Experimental results were presented for a 240 V, 1.68 kVA prototype. The p.u. values from the MV case-study were preserved in the experimental prototype, which enabled direct comparison between experimental and simulation results. The experimental results showed very good agreement with the equivalent simulation results, providing proof-of-concept and indicating that MPDPC is a viable strategy for the control of high-power grid-connected NPC converters.

ACKNOWLEDGMENTS

This work was carried out whilst the first author was with The University of Auckland, New Zealand. This work was also supported in part by The University of Auckland Doctoral Scholarship.

REFERENCES

- [1] J. Maciejowski, *Predictive Control with Constraints*. Harlow, United Kingdom: Prentice Hall, 2002.
- [2] P. Karamanakos, T. Geyer, N. Oikonomou, F. Kieferndorf, and S. Manias, "Direct model predictive control: A review of strategies that achieve long prediction intervals for power electronics," *IEEE Ind. Electron. Mag.*, vol. 8, no. 1, pp. 32–43, Mar. 2014.
- [3] S. Vazquez, J. Leon, L. Franquelo, K. Rodriguez, H. Young, A. Marques, and P. Zanchetta, "Model predictive control: A review of its applications in power electronics," *Ind. Electron. Mag.*, vol. 8, no. 1, pp. 16–31, Mar. 2014.
- [4] H. Young, M. Perez, J. Rodriguez, and H. Abu-Rub, "Assessing finite-control-set model predictive control: A comparison with a linear current controller in two-level voltage source inverters," *IEEE Ind. Electron. Mag.*, vol. 8, no. 1, pp. 44–52, Mar. 2014.
- [5] D. Quevedo, R. Aguilera, and T. Geyer, "Predictive control in power electronics and drives: Basic concepts, theory, and methods," in *Adv. Int. Contr. Power Electron. Drives*, ser. Studies in Computational Intelligence. Springer International Publishing, 2014, vol. 531, pp. 181–226.
- [6] R. Ramirez, J. Espinoza, F. Villarroel, E. Maurelia, and M. Reyes, "A novel hybrid finite control set model predictive control scheme with reduced switching," *IEEE Trans. Ind. Electron.*, vol. 61, no. 11, pp. 5912–5920, Nov. 2014.
- [7] J. Rodriguez, J. Pontt, C. Silva, P. Cortes, U. Amman, and S. Rees, "Predictive current control of a voltage source inverter," *IEEE Trans. Ind. Electron.*, vol. 54, no. 1, pp. 495–503, Feb. 2007.
- [8] J. Rodriguez, M. Kazmierkowski, J. Espinoza, P. Zanchetta, H. Abu-Rub, H. Young, and C. Rojas, "State of the art of finite control set model predictive control in power electronics," *IEEE Trans. Ind. Informat.*, vol. 9, no. 2, pp. 1003–1016, May 2013.
- [9] P. Cortes, S. Kouro, B. La Rocca, R. Vargas, J. Rodriguez, J. Leon, S. Vazquez, and L. Franquelo, "Guidelines for weighting factors design in model predictive control of power converters and drives," in *Proc. IEEE Int. Conf. Ind. Technol.*, Gippsland, Australia, Feb. 2009, pp. 1–7.
- [10] R. Vargas, P. Cortes, U. Ammann, J. Rodriguez, and J. Pontt, "Predictive control of a three-phase neutral-point-clamped inverter," *IEEE Trans. Ind. Electron.*, vol. 54, no. 5, pp. 2697–2705, Oct. 2007.
- [11] J. Rodriguez, J. Pontt, P. Correa, P. Lezana, and P. Cortes, "Predictive power control of an AC/DC/AC converter," in *Proc. IEEE Ind. Appl. Soc. Ann. Meeting*, vol. 2, Hong Kong, Oct. 2005, pp. 934–939.
- [12] P. Cortes, J. Rodriguez, P. Antoniewicz, and M. Kazmierkowski, "Direct power control of an AFE using predictive control," *IEEE Trans. Power Electron.*, vol. 23, no. 5, pp. 2516–2523, Sep. 2008.
- [13] Y. Zhang, W. Xie, Z. Li, and Y. Zhang, "Low-complexity model predictive power control: Double-vector-based approach," *IEEE Trans. Ind. Electron.*, vol. 61, no. 11, pp. 5871–5880, Nov. 2014.
- [14] V. Yaramasu and B. Wu, "Model predictive decoupled active and reactive power control for high-power grid-connected four-level diode-clamped inverters," *IEEE Trans. Ind. Electron.*, vol. 61, no. 7, pp. 3407–3416, Jul. 2014.
- [15] S. Larrinaga, M. Vidal, E. Oyarbide, and J. Apraiz, "Predictive control strategy for DC/AC converters based on direct power control," *IEEE Trans. Ind. Electron.*, vol. 54, no. 3, pp. 1261–1271, Jun. 2007.
- [16] S. Larrinaga, "Predictive control of the 2L-VSI and 3L-NPC VSI based on direct power control for MV grid-connected power applications," Ph.D. dissertation, Faculty of Engineering, University of Mondragon, 2007.
- [17] P. Antoniewicz and M. Kazmierkowski, "Virtual-flux-based predictive direct power control of AC/DC converters with online inductance estimation," *IEEE Trans. Ind. Electron.*, vol. 55, no. 12, pp. 4381–4390, Dec 2008.
- [18] T. Noguchi, H. Tomiki, S. Kondo, and I. Takahashi, "Direct power control of PWM converter without power-source voltage sensors," *IEEE Trans. Ind. Appl.*, vol. 34, no. 3, pp. 473–479, May/Jun. 1998.
- [19] V. Yaramasu, M. Rivera, M. Narimani, B. Wu, and J. Rodriguez, "Model predictive approach for a simple and effective load voltage control of four-leg inverter with an output LC filter," *IEEE Trans. Ind. Electron.*, vol. 61, no. 10, pp. 5259–5270, Oct. 2014.
- [20] C. Rojas, J. Rodriguez, F. Villarroel, J. Espinoza, C. Silva, and M. Trincado, "Predictive torque and flux control without weighting factors," *IEEE Trans. Ind. Electron.*, vol. 60, no. 2, pp. 681–690, Feb. 2013.

- [21] T. Geyer, "Low complexity model predictive control in power electronics and power systems," Ph.D. dissertation, Automatic Control Laboratory, ETH Zurich, 2005.
- [22] T. Geyer, G. Papafotiou, and M. Morari, "Model predictive direct torque control - part I: Concept, algorithm and analysis," *IEEE Trans. Ind. Electron.*, vol. 56, no. 6, pp. 1894–1905, Jun. 2009.
- [23] G. Papafotiou, J. Kley, K. Papadopoulos, P. Böhren, and M. Morari, "Model predictive direct torque control - part II: Implementation and experimental evaluation," *IEEE Trans. Ind. Electron.*, vol. 56, no. 6, pp. 1906–1915, Jun. 2009.
- [24] T. Geyer, "Generalized model predictive direct torque control: Long prediction horizons and minimization of switching losses," in *Proc. IEEE Conf. Decis. Control*, Shanghai, China, Dec. 2009, pp. 6799 – 6804.
- [25] T. Geyer, "Computationally efficient model predictive direct torque control," *IEEE Trans. Power Electron.*, vol. 26, no. 10, pp. 2804–2816, Oct. 2011.
- [26] T. Geyer, "Model predictive direct current control: Formulation of the stator current bounds and the concept of the switching horizon," *IEEE Ind. Appl. Mag.*, vol. 18, no. 2, pp. 47–59, Mar. 2012.
- [27] T. Geyer, J. Scoltock, and U. Madawala, "Model predictive direct power control for grid-connected converters," in *Proc. IEEE Ind. Electron. Soc. Conf.*, Melbourne, Australia, Nov. 2011, pp. 1438 – 1443.
- [28] S. Alepuz, S. Busquets-Monge, J. Bordonau, J. Martinez-Velasco, C. Silva, J. Pontt, and J. Rodriguez, "Control strategies based on symmetrical components for grid-connected converters under voltage dips," *IEEE Trans. Ind. Electron.*, vol. 56, no. 6, pp. 2162–2173, Jun. 2009.
- [29] F.-Z. Peng and J.-S. Lai, "Generalized instantaneous reactive power theory for three-phase power systems," *IEEE Trans. Inst. Meas.*, vol. 45, no. 1, pp. 293–297, Feb. 1996.
- [30] T. Geyer, "A comparison of control and modulation schemes for medium-voltage drives: Emerging predictive control concepts versus PWM-based schemes," *IEEE Trans. Ind. Appl.*, vol. 47, no. 3, pp. 1380–1389, May/Jun. 2011.
- [31] *IEEE recommended Practices and Requirements for Harmonic Control in Electrical Power Systems*, IEEE 519-1992 Std., 1993.
- [32] B. Bahrani, A. Karimi, B. Rey, and A. Rufer, "Decoupled dq -current control of grid-tied voltage source converters using nonparametric models," *IEEE Trans. Ind. Electron.*, vol. 60, no. 4, pp. 1356–1366, Apr. 2013.
- [33] B. McGrath, D. Holmes, and T. Lipo, "Optimized space vector switching sequences for multilevel inverters," *IEEE Trans. Power Electron.*, vol. 18, no. 6, pp. 1293–1301, Nov. 2003.
- [34] P. Cortes, J. Rodriguez, C. Silva, and A. Flores, "Delay compensation in model predictive current control of a three-phase inverter," *IEEE Trans. Ind. Electron.*, vol. 59, no. 2, pp. 1323–1325, Feb. 2012.
- [35] T. Geyer and D. Quevedo, "Performance of multistep finite control set model predictive control for power electronics," *IEEE Trans. Power Electron.*, vol. 30, no. 3, pp. 1633–1644, Mar. 2015.
- [36] H. Peyrl, S. Richter, and A. Zanarini, "Multi-core parallelisation of integer optimisation model predictive control for power electronic applications," in *Proc. Eur. Contr. Conf.*, Zurich, Switzerland, Jul. 2013, pp. 1511–1516.
- [37] T. Geyer, R. Aguilera, and D. Quevedo, "On the stability and robustness of model predictive direct current control," in *Proc. IEEE Int. Conf. Ind. Techn.*, Cape Town, South Africa, Feb. 2013, pp. 374–379.



James Scoltock (S'09 - M'15) completed the B.E. (Hons) and Ph.D. degrees, both in electrical and electronic engineering, at The University of Auckland, New Zealand, in 2009 and 2015, respectively. He is currently a Research Associate with the School of Electrical and Electronic Engineering, The University of Manchester, United Kingdom. His research interests include power electronics, electrical drives, and model predictive control.



Tobias Geyer (M08-SM10) received the Dipl.-Ing. and Ph.D. degrees in electrical engineering from ETH Zurich, Zurich, Switzerland, in 2000 and 2005, respectively.

From 2006 to 2008, he was with the High Power Electronics Group of GE's Global Research Centre, Munich, Germany, where he focused on control and modulation schemes for large electrical drives. Subsequently, he spent three years at the Department of Electrical and Computer Engineering, The University of Auckland, Auckland, New Zealand, where he developed model predictive control schemes for medium-voltage drives.

In 2012, he joined ABBs Corporate Research Centre, Baden-Dttwil, Switzerland. His research interests are at the intersection of power electronics, modern control theory and mathematical optimization. This includes model predictive control and medium-voltage ac drives.

Dr. Geyer was a recipient of two Prize Paper Awards at conferences and of the 2014 Third Best Paper Award of the Transactions on Industry Applications. From 2011 until 2014 he served as an Associate Editor of the Industrial Drives Committee for the Transactions on Industry Applications. Since 2013 he has been serving as an Associate Editor for the Transactions on Power Electronics. He has authored and co-authored more than 100 peer-reviewed publications and patent applications.



Udaya K. Madawala (M'95 - SM'06) received the B.Sc. (Hons.) degree in electrical engineering from the University of Moratuwa, Moratuwa, Sri Lanka, and the Ph.D. degree in power electronics from the University of Auckland, Auckland, New Zealand, in 1987 and 1993, respectively.

After working in industry, he joined the Department of Electrical and Computer Engineering, University of Auckland as a Research Fellow in 1997, where he is currently a Professor. His research interests include power electronics, inductive power transfer, and renewable energy.

Dr. Madawala is an active IEEE volunteer, and serves as an Associate Editor for the IEEE TRANSACTIONS ON INDUSTRIAL ELECTRONICS and the IEEE TRANSACTIONS ON POWER ELECTRONICS. He is a Member of the Power Electronics Technical Committee of the IEEE Industrial Electronics Society and the Sustainable Energy Systems Committee of the IEEE Power Electronics Society.